X International Conference on Computational Methods in Marine Engineering
MARINE 2023
J. Garcia-Espinosa, L. González, J.E. Gutiérrez & B. Serván-Camas (Editors)

Numerical Investigation on Transitional Boundary Layer of Submarine with Different Bow Shapes

Xinxin Meng[1], Liushuai Cao[1], Zhiben Shen[2], Yun Wang[2], Decheng Wan[1]*

[1] Computational Marine Hydrodynamics Lab (CMHL), School of Naval Architecture, Ocean and Civil Engineering, Shanghai Jiao Tong University, Shanghai, China.

[2] Wuhan Second Ship Design and Research Institute,Wuhan,China

*Corresponding Author: dcwan@sjtu.edu.cn

ABSTRACT

The shape of a submarine bow affects the transition point of the boundary layer, and an excellent bow profile will delay the transition, thus improving the resistance performance, reducing hydrodynamic noise, which will benefit the stealth of the submarine. With the development of computational fluid dynamics (CFD), high-fidelity numerical simulation of transitional boundary layer near the bow is urgent, seeking to determine the best shape of the bow. First, the research status of boundary layer transition modeling methods is reviewed. Then, multi-block based structured grid and large eddy simulation (LES) are adopted to simulate the natural transition of different bow shapes. Vortex structures, transition point, skin friction, and pressure fluctuations are analyzed and compared. Finally, the best shape of submarine bow is chosen for subsequent research.

Keywords: Submarine; Transitional boundary layer; Bow shape; LES; CFD

1. INTRODUCTION

Boundary layer transition is the phenomenon of laminar-to-turbulent flow transition that manifests through turbulent bursts or spots in the boundary layer transition zone, leading to the eventual development of fully turbulent flow. The transition of the boundary layer is influenced by various factors, including roughness, bow shape, flow velocity, and environmental conditions. Four types of transition have been identified, namely T-S wave transition, cross-flow transition, vortex shedding transition, and attachment-line transition. Boundary layer transition is a crucial phenomenon that occurs within the boundary layer, and for submarines, the bow boundary layer transition represents a critical fluid mechanics problem with significant engineering implications. Research suggests that the transition zone emits relatively strong sound radiation, which is significant for practical engineering problems. Although some studies have examined the influence of bow shape on the transition, flow field analysis is not the primary means of determination for most studies.

Tabatabaei et al. (2021) utilized the RANS method and a modified model to predict the transition phenomenon, and compared their results with those obtained using DNS and LES methods. While the RANS method and stability analysis method are computationally efficient and do not require a detailed flow field grid, they provide an indirect means of analyzing specific variables. Conversely, the LES and DNS methods can simulate linear and nonlinear processes of perturbations and possess strong transition prediction capabilities. To accurately predict the transition position and understand the underlying mechanisms, this study adopted the LES method, which enables precise simulation while reasonably controlling computational time and volume. By directly analyzing the flow field, the LES method can determine the onset position of transition and the position where it develops into fully turbulent flow. This approach effectively avoids errors caused by data conversion and ensures accurate determination of the transition occurrence.

Various analytical methods are available to investigate the boundary layer, with Reynolds number being the most significant parameter to characterize the flow regime within it. Typically, the flow in the boundary layer remains laminar when the Reynolds number is below 2×10^5. However, if the Reynolds number exceeds this threshold, the boundary layer is prone to transition to turbulent flow. In research on how Reynolds number

affects the boundary layer over axisymmetric bodies L^*, turbulent flow fields are commonly studied. The target Reynolds numbers are generally less than Re_D of 10^7, corresponding to a body-length Reynolds number (Re_L) of less than 10^8, as in the experiment conducted by Mitra et al. (2019), which studied the turbulent flow over an axisymmetric body in a water tank at three Reynolds numbers ($Re_D \leqslant 1.0 \times 10^5$).

Lee and Jones (2020) investigated turbulent boundary layer separation on an axisymmetric body using wind tunnel experiments with Re_L ranging from 4.2×10^6 to 1.7×10^7.

Posa and Balaras (2020) employed large-eddy simulation to study the turbulent flow field over an axisymmetric body. First, they calculated the turbulent boundary layer at the Reynolds number corresponding to the laboratory model ($Re_L = 1.2 \times 10^6$) and found these results to be consistent with experimental results. Then, Posa and Balaras (2020) increased the Reynolds number by a factor of 10 to $Re_L = 1.2 \times 10^7$ to observe its effects on the flow field.

Axisymmetric body shapes are commonly employed in underwater vehicles due to their hydrodynamic advantages (Wang et al., 2022; Xuan et al., 2022). However, the transition location in the boundary layer over such bodies can significantly affect flow noise (Li et al., 2011; Liu et al., 2018; Huang et al., 2019), which, in turn, can impact sonar detection at the nose. Therefore, understanding transitions over underwater axisymmetric bodies is of paramount importance.

Yang et al. (2018) provided a comprehensive summary of previous research on the transition problem, including the types of transition, special structures in the transition zone, and transition prediction methods. They recommended employing multiple techniques to study the transition mechanism and predicted that future transition research will focus on predicting three-dimensional boundary layer transitions on objects. Yang et al. also proposed scaling laws to understand the transition mechanism.

Liu et al. (2021) employed the e^N method to investigate the boundary layer transition phenomenon of underwater rotating bodies with different bow shapes. Their analysis of seven bow shapes demonstrated that different shapes corresponded to different transition points. Furthermore, the transition location of the same model under different working conditions could be altered. Numerical simulation results showed that the flow states of different models tended to converge after two times the length of the model's head.

Overall, this body of research highlights the importance of understanding the transition mechanism over underwater axisymmetric bodies and the need to employ multiple methods to study the problem comprehensively. The findings of Liu et al. offer valuable insights into the effect of bow shape on boundary layer transition, which can inform the design of underwater vehicles.

Furthermore, a comprehensive understanding of the impact of Reynolds number on the transition of underwater axisymmetric bodies, especially over a wide range of Reynolds numbers, remains elusive. This is further complicated by the fact that the laminar basic flows lack similarity for underwater axisymmetric bodies compared to flat-plate boundary layers. Despite some relevant studies conducted in the low-Reynolds-number range (Arakeri, 1975 and Liu et al., 2021), the transition locations in the boundary layers of underwater axisymmetric bodies at high Reynolds numbers and the influence of Reynolds number changes on natural transition are still an active area of research. This research is of great scientific significance and is a critical topic in the field of fluid mechanics.

In this study, we employ large eddy simulation (LES) to investigate the phenomenon of SUBOFF bow transition at high Reynolds numbers and analyze its underlying mechanism. To explore the effect of bow shape on the transition, we vary the shape of the bow and utilize multiple methods to analyze the transition location of the bow in various models. Furthermore, we use spectral analysis to investigate the impact of different bow shapes on the transition. The combination of these approaches enables us to gain a comprehensive understanding of the transition mechanism and the influence of bow shape on the phenomenon. This research

provides significant insights into the fundamental understanding of flow transitions in underwater axisymmetric bodies and can be useful for optimizing the design of underwater vehicles.

2. NUMERICAL METHOD

2.1 Governing equations

In the Cartesian coordinate system, the continuity equation and Navier-Stokes equations for viscous, incompressible fluids using Reynolds averaging are expressed as:

$$\frac{\partial \overline{u_i}}{\partial x_i} = 0 \tag{1}$$

$$\frac{\partial(\rho\bar{u}_i)}{\partial t} + \bar{u}_j \frac{\partial(\rho\bar{u}_i)}{\partial x_j} = -\frac{\partial \bar{P}}{\partial x_j} + \mu \frac{\partial}{\partial x_j}\left(\frac{\partial \bar{u}_i}{\partial x_j} - \rho\overline{u_i u_j}\right) \tag{2}$$

In the equations: $i, j = 1,2$; ρ is the air density, ρ=$10^3\ kg \cdot m^{-3}$; μ is the dynamic viscosity coefficient, μ=$1.0\times10^6\ kg \cdot m^{-1} \cdot s^{-1}$.

2.2 Numerical Methods

This section presents the turbulence model selected for this study, namely the LES WALE model.

Firstly, the spatial filtering operator is defined as:

$$\widetilde{U}_i(\boldsymbol{x}, t) = \int G(\boldsymbol{x} - \boldsymbol{x}')U_i(\boldsymbol{x}', t)\mathrm{d}\boldsymbol{x}' = \mathbb{G}U_i(\boldsymbol{x}, t) \tag{3}$$

where G is the spatial filtering function. For convenience, G is used to represent the filtering operator. $U(x, t)$ represents the large-scale part of the velocity field after filtering. To distinguish it from the Reynolds-averaged velocity $\overline{U}_i$, it is represented as $\widetilde{U}_i$.

The continuity equation for large eddy simulation is expressed as:

$$\frac{\partial \widetilde{U}_i(\boldsymbol{x}, t)}{\partial x_i} = 0 \tag{4}$$

Filtering operation is applied to the Navier-Stokes equation, and the linear term is easy to deal with. The nonlinear term is temporarily represented by A_{ij}. Thus, we have:

$$\frac{\partial \widetilde{U}_i}{\partial t} + \frac{\partial A_{ij}}{\partial x_j} = -\frac{1}{\rho_0}\frac{\partial \tilde{P}}{\partial x_i} + \nu \cdot \nabla^2 \widetilde{U}_i \tag{5}$$

Subsequently, the Navier-Stokes equation for large eddy simulation can be obtained as follows:

$$\frac{\partial \widetilde{U}_i}{\partial t}+\frac{\partial\left(\widetilde{U}_i \widetilde{U}_j\right)}{\partial x_j}=-\frac{1}{\rho_0}\frac{\partial \tilde{P}}{\partial x_i}-\frac{\partial L_{ij}}{\partial x_j}-\frac{\partial S_{ij}}{\partial x_j}+\nu\cdot\nabla^2\widetilde{U}_i \tag{6}$$

To solve this equation, L_{ij} and S_{ij} must be given. L_{ij} is called the Leonard stress, which is a small quantity dependent on the filtering function. Choosing an appropriate filtering function can make $L_{ij}\approx 0$. In fact, the Leonard stress may be masked by errors in numerical calculations, so it can be ignored.

S_{ij} is known as the subgrid-scale Reynolds stress, which is related to the unresolved subgrid-scale motions. This quantity affects the large-scale motion and the equation is not closed without specifying this term. For the LES WALE model, it is typically described by a model:

$$S_{ij}=-\mu_t\left(\frac{\partial \widetilde{U}_i}{\partial x_j}+\frac{\partial \widetilde{U}_j}{\partial x_i}\right) \tag{7}$$

The subgrid equivalent dynamic viscosity coefficient is given by:

$$\mu_t=\rho L_s^2\frac{\left(S_{ij}^d S_{ij}^d\right)^{3/2}}{\left(\tilde{S}_{ij}\tilde{S}_{ij}\right)^{5/2}+\left(S_{ij}^d S_{ij}^d\right)^{5/4}} \tag{8}$$

The stress term and parameters in the equation are calculated by the following expressions:

$$\tilde{S}_{ij}=\frac{1}{2}\left(\frac{\partial \widetilde{U}_i}{\partial x_j}+\frac{\partial \widetilde{U}_j}{\partial x_i}\right) \tag{9}$$

$$S_{ij}^d=\frac{1}{2}\left(\bar{g}_{ij}^2+\bar{g}_{ji}^2\right)-\frac{1}{3}\delta_{ij}\bar{g}_{kk}^2, \bar{g}_{ij}=\frac{\partial \bar{u}_i}{\partial x_j} \tag{10}$$

$$Ls=min(\kappa d, C_W\Delta) \tag{11}$$

The parameter C_{W} is a dimensionless coefficient of the WALE model, which typically takes a value of $C_{\mathrm{W}}=0.5$.

3 Verification of Computational Methods

In this section, the inner solver pisoFoam in OpenFOAM is used to simulate the boundary transition of the bow of submarine. Firstly, the stability and accuracy of the computational method were validated using a scale model test case (SUBOFF) and compared against experimental data.

3.1 Computational Domain and Mesh Generation

The LES methodology necessitates higher grid quality in the near-wall region, which is addressed via utilization of structured grids facilitating the generation of 15 layers of boundary cells. The total grid number is approximately 13 million cells, with the respective grid parameters presented in the accompanying Table.1：

Table 1. Grid parameter

parameter	value
Total grid number/million	13
Minimum unit size/m	9.0e-06
Numbers of layer	15
y^+	1

The SUBOFF model has a length of 4.356m, with a computational domain ranging from -10 m to 40 m in the x-direction, -10 m to 10 m in the y-direction, and -10 m to 10 m in the z-direction.

3.2 Validation and Analysis of Computational Results

Validation is mainly carried out through two approaches: (1) comparison of computational results with experimental data, which is primarily accomplished through verification of two dimensionless coefficients obtained from calculations, namely$C_p = p/0.5\rho U_\infty^2$ and $C_f = \tau_w /0.5\rho U_\infty^2$; (2) comparison of computational results with empirical formulas, where the time history curve of fluctuating pressure at a particular point is computed and compared with experimental data(Peng et al., 2001) obtained by previous researchers.

The SUBOFF model was computed under the operating conditions listed in the following Table 2 and compared with experimental data:

Table 2. Computational operating conditions

parameter	value
Length/m	4.356
Inter speed m/s	2.8368
Re_L	1.24× 10^7

3.2.1 Verification of Time-Averaged Coefficients

The accuracy of the computational method was verified by comparing it with experimental data, as shown in Figure 1. The comparison of C_f and C_p coefficients indicates that the pressure coefficients obtained from large eddy simulation (LES) calculations are in good agreement with those obtained from experiments, with a maximum error of no more than 5%. The overall error of the friction coefficient is also relatively small. These results suggest that the numerical simulation method is accurate and that LES can reflect the actual situation well.

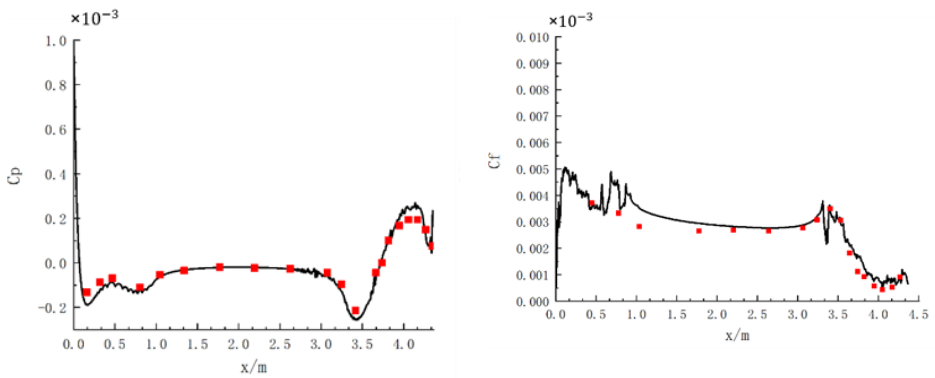

(a) (b)

Figure 1 (a) coefficient of pressure and (b) coefficient of shear stress

3.2.2 The Fields of Velocity and Pressure

The following is the relevant information of the fields, including the velocity field and pressure field.

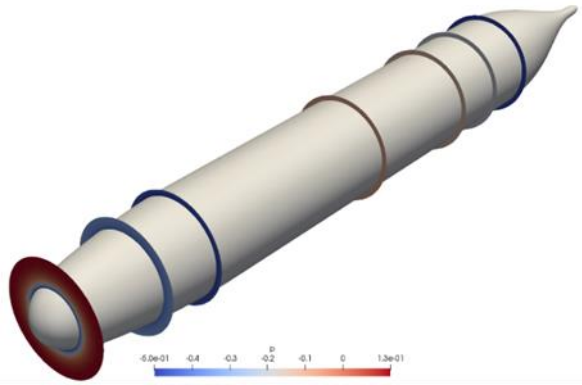

(a)

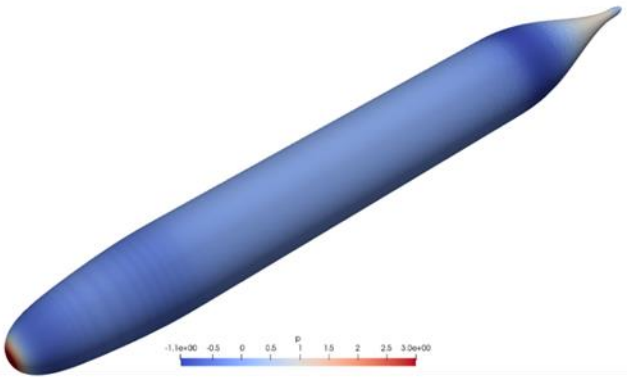

(b)

(c)

Figure 2 (a) Positions schematic diagram of seven toroidal, (b)Pressure distribution of the hull and (c)Development of flow velocity in the streamwise direction

Seven toroidal sections were taken along the hull, at x=0.1; 0.5; 0.8; 2; 2.7; 3; 3.3m. Preliminary observations of the velocity profiles along several toroidal sections indicate that the velocity within the boundary layer evolves in the streamwise direction. Small velocity perturbations were observed at x=2, while significant perturbations were observed at x=3. As for the pressure distribution, significant pressure fluctuations were observed at the stern of the hull, with slight pressure fluctuations between (2.7, 3). No pressure fluctuations were observed at x < 2.7, though the actual transition location may occur earlier. Therefore, the observations serve only as a supplementary judgment, and further analysis will be conducted based on the data.

3.2.3 Statistical Analysis

We selected 206 pressure measurement points along the streamline direction to obtain the variation of pressure on the hull surface with time, and calculated the root mean square (RMS) pressure value at each point using statistical analysis.

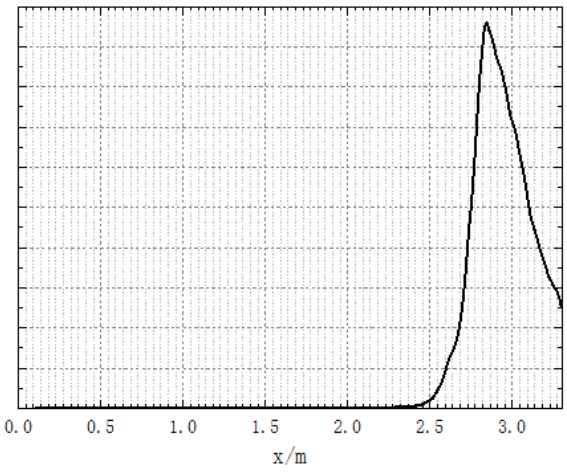

Figure 3 The curve of RMS of fluctuating pressure

According to the Figure 3, it can be seen that for the SUBOFF: the pressure fluctuation is extremely small when x is less than 2.35. When x is between 2.35 and 2.5, the pressure fluctuation increases slowly. When x is greater than 2.5, the pressure fluctuation increases rapidly, reaching its maximum value around x=2.8 and then decreasing rapidly. Flow separation occurs after x=3.3 and will not be discussed here. Therefore, it can be preliminarily concluded that the transition zone of the standard model SUBOFF obtained by large eddy simulation method is approximately (2.35, 3.3). There are 60 measurement points arranged in this zone, and 6 typical measurement points are selected for discussion, as shown in Table 3:

Table 3. Information for typical measurement points

Item	Unit	(1)	(2)	(3)	(4)	(5)	(6)
X-axis	m	2.360	2.656	2.781	2.813	2.984	3.297
Amplitude of pressure	Pa	0.32	21.24	122.22	199.84	186.39	64.50

It can be observed that at the onset of transition in the Figure 4, the pulsatile pressure was not significant, and the power spectral density showed a trend similar to that of laminar flow. Subsequently, the pulsatile pressure increased, and both the low and high frequency components increased rapidly until x=2.8. Afterwards, the high frequency component continued to increase, while the low frequency component decreased slightly. It can be tentatively concluded that the low frequency component is higher in the transition region, which is consistent with the location of the maximum root-mean-square value.

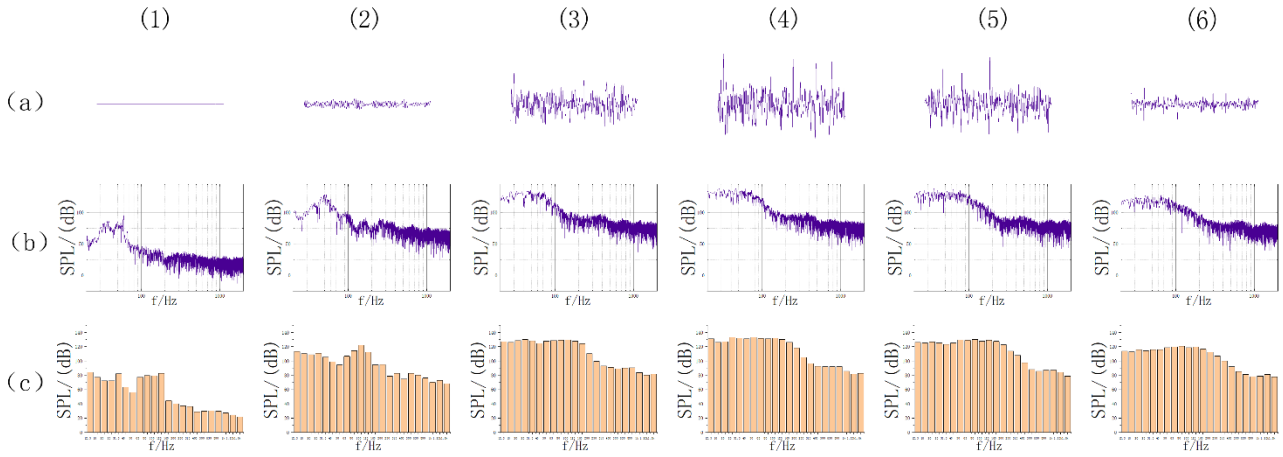

Figure 4 (a) Pulsatile Pressure Time History Curve, (b) Power Spectral Density, (c) 1/3 Octave Band Spectrum

Summary

In this chapter, the accuracy of large eddy simulation (LES) method was validated using the SUBOFF. Additionally, by applying statistical analysis methods, the transition range of SUBOFF was determined, laying the foundation for the subsequent qualitative analysis of the influence of the submarine bow on boundary layer

4. Investigating the Influence of Bow Form on Transition

The correctness of the calculation method has been verified in the previous chapter. In this chapter, the verified method is applied to calculate the influence of different bow forms of the submarine on transition.

4.1 Three Types of Forms

To analyze the effect of the shape of the submarine's bow on its turning performance, two different line shapes were drawn based on the bow shape of SUBOFF. The comparison of these two line shapes is shown in the following figure, where each line shape corresponds to a specific function that satisfies the following conditions: (1) $f(0) = 0$; (2) $f'(0) = \infty$; (3) $f(a) = 1$; (4) $f'(a) = 0$, where a is the starting point of the parallel mid-body, (2) represents a smooth bow section, and (3) represents that all three line shapes correspond to the same width of the parallel mid-body.

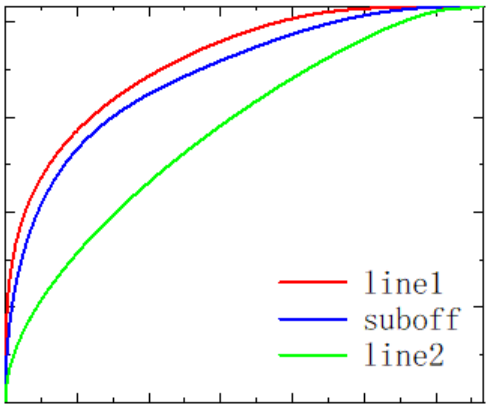

Figure 5 Line diagrams of three types of bow forms

From the figure 5, it can be observed that line 1 is similar in shape to SUBOFF, but with slight differences. The bow shape of line 2 is sharper and differs significantly from the other two-line types. All three curves are extremely smooth. Since, beyond twice the headway distance, different line types correspond to similar flow fields (Peng et al., 2001), the same parallel mid-body and stern shapes as SUBOFF are employed for the other two-line types to study the effects of the bow shape on the flow field using a controlled variable method.

4.2 Effects of Different Bow Shapes on Transition

In order to provide a comprehensive analysis, this section will examine the topic from three perspectives: (1) analysis of the maximum values for the three types of shapes; (2) data analysis for Line 1; and (3) data analysis for Line 2.

4.2.1 Analysis of Maximum Values

Firstly, a comparison of the root mean square (RMS) values was conducted, and then the spectra and 1/3 octave spectra were compared at the RMS maximum values for different bow shapes, in order to analyze the effects of different bow shapes on transition. As shown in Figure 6(a), the three shapes had similar RMS maximum values for fluctuating pressure, indicating that for transition, the maximum value of data fluctuations can be predicted. However, the trends for different shapes were different, indicating that bow shape can affect

transition: (1) A comparison between SUBOFF and Line 2 shows that the time from when the data begins to fluctuate until the point of maximum value is different, with Line 2 taking longer from instability to RMS maximum value. Through analysis of the data from SUBOFF, it can be seen that this phenomenon is strongly related to the number of selected data sets. For statistical data similar to the root mean square of pressure, a large amount of stable and reliable data can yield more accurate results. Furthermore, the different RMS peak values corresponding to the three bow shapes are directly due to the change in pressure distribution of the hull caused by the change in bow shape; (2) A comparison between SUBOFF and Line 1 shows that the overall rate of decrease for the corresponding value of Line 1 after reaching the RMS maximum value is significantly lower than that of SUBOFF, and there is a phenomenon of secondary increase during the decrease process, which is also related to the bow shape; (3) From Figure 6(b) and (c), it can be seen that the numerical values and trends of the spectra for the three shapes are almost identical, while the 1/3 octave spectra show that Line 1 is greater than Line 2 and SUBOFF in the frequency range of 80Hz to 315Hz, indicating that the bow shape not only affects the magnitude of pressure but also influences the frequency distribution.

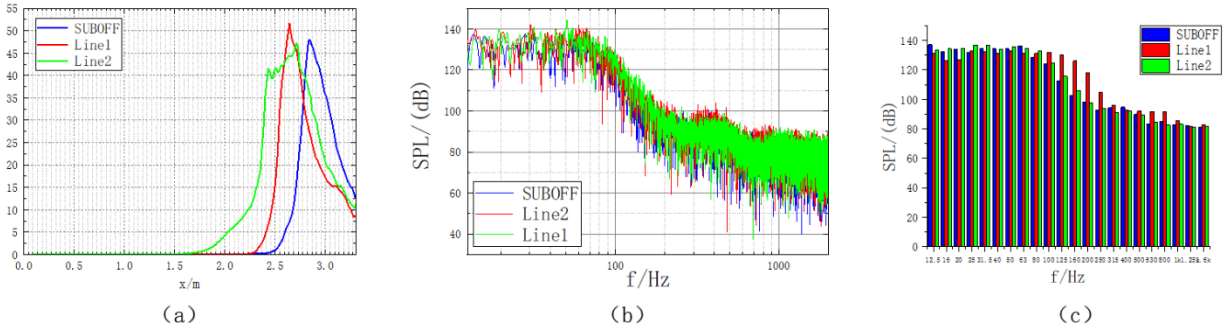

Figure 6 (a) Variation of Root Mean Square along the flow direction, (b) Pressure spectrum and (c) 1/3 octave spectrum.

4.2.2 Data Analysis of Line 1 and Line2 Profile

Based on the calculation results of SUBOFF in Chapter 3, we adopted the same method to select six representative measurement points. Table 4. and Table 5. presents the corresponding data for these six points for Line1 and Line2.

Through the comparison between Line1 and Line2, we have observed an interesting phenomenon: Figures 7(a)-(3) and Figures 8(a)-(3) exhibit two different development trends over time. Line2 shows clear periodicity, while Line1 and SUBOFF show no apparent periodic behavior. This indicates that the bow shape of Line2 does not disrupt the development of near-wall vortex structures. From Figures 4(c), 7(c), and 8(c), it can be seen that as the x-coordinate increases, the octave spectra show an initial increase followed by a decrease. This suggests that the overall sound pressure level in the transition region is higher than that in the fully turbulent region and laminar region.

Table 4. Information for typical measurement points of Line1

Item	Unit	(1)	(2)	(3)	(4)	(5)	(6)
X-axis	m	2.200	2.422	2.531	2.631	2.838	3.278
Amplitude of pressure	Pa	0.43	6.83	220.96	166.83	95.66	63.52

Table 5. Information for typical measurement points of Line2

Item	Unit	(1)	(2)	(3)	(4)	(5)	(6)
X-axis	m	1.570	1.914	2.383	2.695	2.977	3.305
Amplitude of pressure	Pa	0.24	13.33	75.71	207.08	118.05	45.56

As can be seen from the Table 4, unlike the pattern observed in SUBOFF, the maximum fluctuation pressure at the location of the root mean square maximum value of x is not the highest in the flow direction; rather, the maximum fluctuation pressure is achieved before this point where the amplitude of fluctuation pressure is the highest. This interesting phenomenon indicates that pressure fluctuations are more intense and irregular before the root mean square value reaches its maximum, as also concluded from row (3) of panel (a) in Figure 8. In addition, only the (a) series in Figure 8 exhibits a similar trend to SUBOFF. For (b), it can be observed that the spectral levels do not rapidly increase in the low-frequency range as x increases; instead, the growth of both low- and high-frequency components is almost synchronous. A decrease in both low- and high-frequency components is observed when $x \approx 3.3$. For (c), the trend is almost identical and the values are much higher than those of SUBOFF. This indicates that the variation of fluctuation pressure does not directly affect noise in the case of the Line1 model, and the bow shape of the profile may be a factor affecting the noise, as the 1/3-octave spectrum starts to exhibit the trend shown in (c) from the bow.

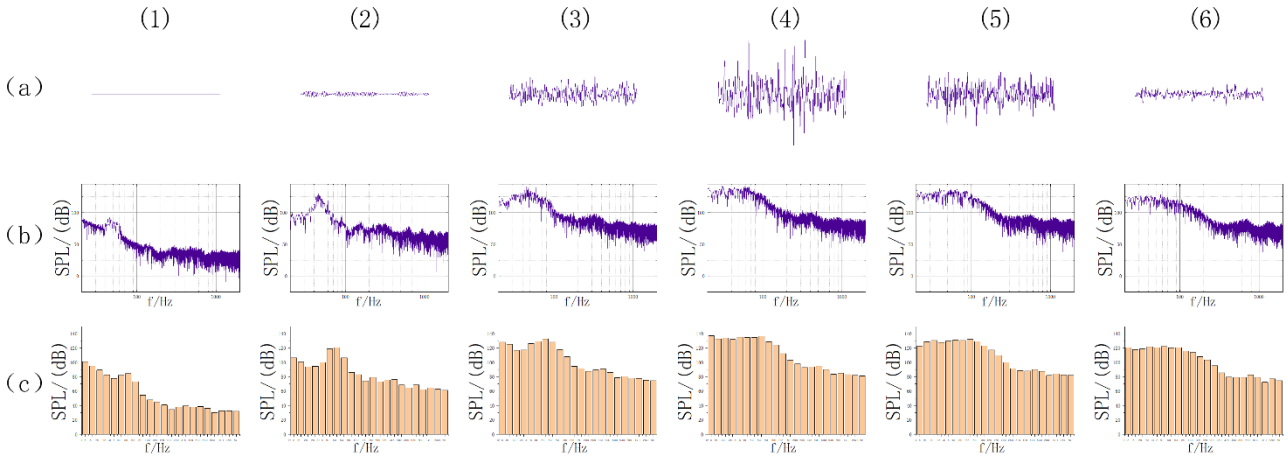

Figure 7 （a）Pulsatile Pressure Time History Curve,（b）Power Spectral Density and（c）1/3 Octave Band Spectrum

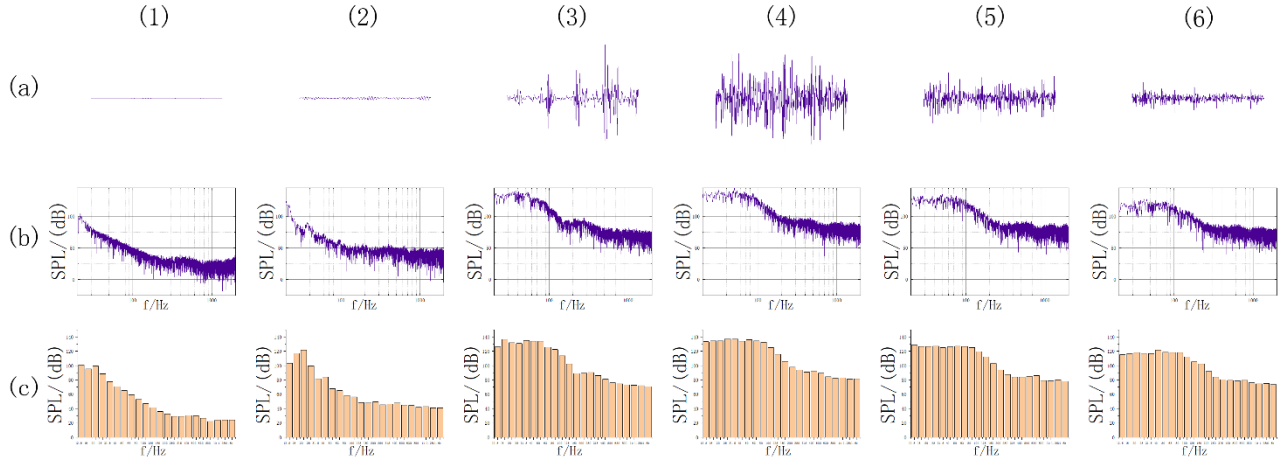

Figure 8 （a）Pulsatile Pressure Time History Curve,（b）Power Spectral Density and（c）1/3 Octave Band Spectrum

4.2.3 Empirical Mode Decomposition

Empirical Mode Decomposition (EMD) is a widely used signal processing method that can also be applied to analyze pulsatile pressure. Here, we employ the EMD approach to specifically examine the impact of header geometry on pulsatile pressure and investigate the mechanism behind the header geometry-induced transition by comparing identical modes. Additionally, we compare the frequency distribution of imf=1, imf=3, and imf=6 for SUBOFF.

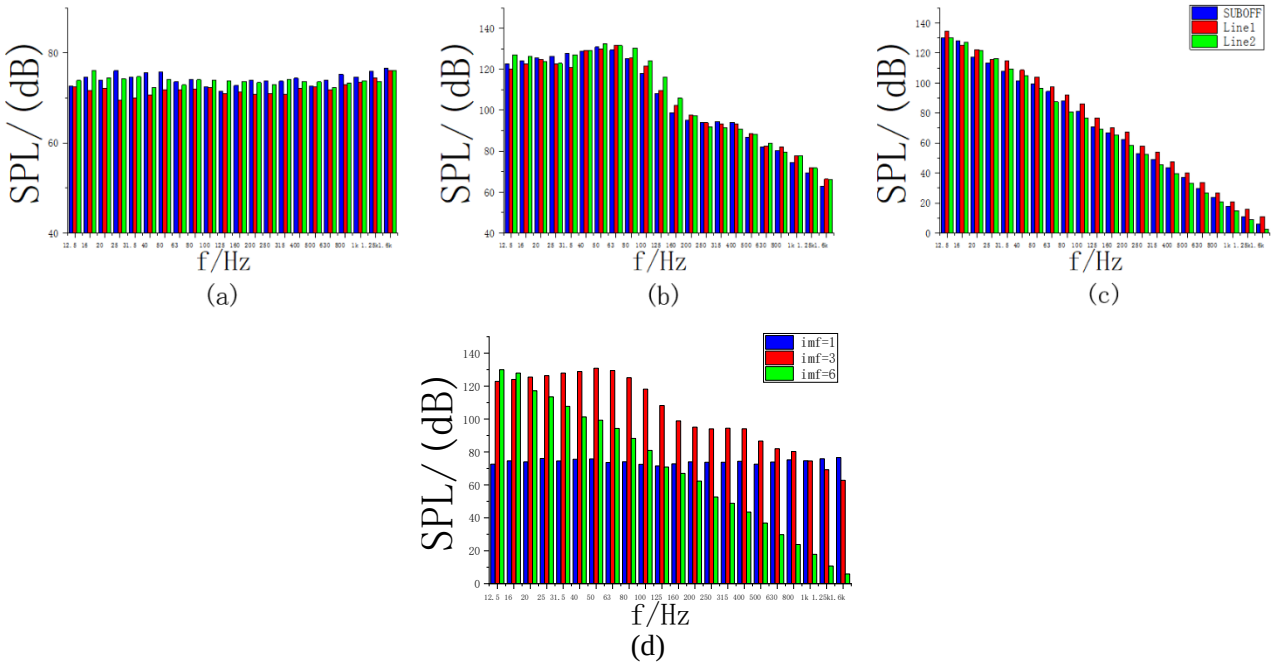

Figure 9 （a）illustrates the one-third octave spectrum plot for imf=1,(b) illustrates the one-third octave spectrum plot for imf=3,(c) illustrates the one-third octave spectrum plot for imf=6, (d) presents a comparison of the three modes of SUBOFF.

By employing empirical mode decomposition, we decompose the pulsatile pressure into various modes ranging from high frequency to low frequency (imf=1 to imf=10). From Figure 9 (d), it can be observed that imf=3 is the dominant mode among the three line geometries. Within the frequency range of this mode, the overall sound pressure level is relatively high. In contrast, imf=1 corresponds to high-frequency components, exhibiting comparable sound pressure levels for both high and low frequencies, indicating its significant contribution to pulsatile pressure. On the other hand, imf=6 represents a low-frequency mode, with remarkably low sound pressure levels in the high-frequency range, suggesting its crucial role in low-frequency noise.

From Figures 9 (a), (b), and (c), it can be observed that the first two modes (imf=1 and imf=3) of Line1 exhibit relatively low sound pressure levels, whereas the third mode (imf=6) demonstrates higher sound pressure levels. This indicates that the line geometry of Line1 influences the pulsatile pressure through its impact on low-frequency modes.

By utilizing the empirical mode decomposition method, we have gained preliminary insights into the mechanism through which the header geometry affects pulsatile pressure and subsequently the transition process. This lays the foundation for our future investigations.

5. CONCLUSIONS

Through numerical simulations of SUBOFF, Line1, and Line2, it has been observed that the bow shape indeed affects the transition point and transition interval. Furthermore, the bow shape also influences the pressure fluctuations and frequency distribution. Lastly, the periodicity observed in the time history curve of Line2 suggests that the bow shape may impact the near-wall vortex structure.

During the numerical simulations, it was found that the transition point obtained through the LES WALE algorithm is further delayed, which could be related to the inflow conditions. In this study, uniform inflow conditions were utilized. In future validations, it would be necessary to investigate the influence of inflow conditions on transition. Moreover, the number of grid cells can also affect the computational results, particularly the number of grid cells in the near-wall boundary layer, which is crucial for capturing small-scale fluctuations.

ACKNOWLEDGEMENTS

This work was supported by the National Natural Science Foundation of China (52131102), and the National Key Research and Development Program of China (2019YFB1704200), to which the authors are most grateful.

REFERENCES

A. Mitra, J.P. Panda, H.V. Warrior (2019). The effects of free stream turbulence on the hydrodynamic characteristics of an AUV hull form. *Ocean Engineering*, 174, 148-158.

Antonio Posa, Elias Balaras (2019). A numerical investigation about the effects of Reynolds number on the flow around an appended axisymmetric body of revolution. *Journal of Fluid Mechanics*, 884, A41.

Jingcheng-Liu, Jianhua-Liu, Yongming-Zhang (2023). Influence of Reynolds number on the natural transition of boundary layers over underwater axisymmetric bodies. *Physics of Fluids* ,35 (4): 044107.

Linhui-Peng, Jianhui-Lu (2001). The Estimation Method for Self Noise of Underwater Fluid-Coming Structure. *Theoretical and Computational Acoustics*, pp. 247-252.

Li Xue-Gang, Yang Kun-De, Wang Yong (2011). The power spectrum and correlation of flow noise for an axisymmetric body in water. *Chinese Physical Society and IOP Publishing Ltd Chinese Physics B*, 20, 1674-1056.

Narges Tabatabaei, Ricardo Vinuesa, Ramis Örlü, Philipp Schlatter (2022). Techniques for Turbulence Tripping of Boundary Layers in RANS Simulations. Flow, *Turbulence and Combustion*, 108, 661–682.

S.-K. Lee, ORCID, M. B. Jones. Surface-pressure pattern of separating flows over inclined slender bodies. *Physics of Fluids*,32, 095123.

V. H. Arakeri (1975). A Note on the Transition Observations on an Axisymmetric Body and Some Related Fluctuating Wall Pressure Measurements. *J. Fluids Eng*., 97(1): 82-86.

Xuehao-Wang, Yanhui-Wang, Peng-Wang, Shaoqiong-Yang, Wendong-Niu, Yehao-Yang. Design, analysis, and testing of Petrel acoustic autonomous underwater vehicle for marine monitoring. *Physics of Fluids*,34, 037115.

YANG Wubing, SHEN Qing, ZHU Dehua, YU Min, LIU Zhiyong (2018). Tendency and current status of hypersonic boundary layer transition. *China Academy of Aerospace Aerodynamics*, 36(2): 183-195.